Article

JPSS-2 VIIRS Pre-Launch Reflective Solar Band Testing and Performance

David Moyer [1,*], Amit Angal [2], Qiang Ji [2], Jeff McIntire [2] and Xiaoxiong Xiong [3]

1 The Aerospace Corporation, El Segundo, CA 90245, USA
2 Science Systems and Applications Inc., Lanham, MD 20706, USA
3 NASA Goddard Space Flight Center, Greenbelt, MD 20771, USA
* Correspondence: david.i.moyer@aero.org

Abstract: The Visible Infrared Imaging Radiometer Suite (VIIRS) instruments on-board the Suomi National Polar-orbiting Partnership (S-NPP) and Joint Polar Satellite System (JPSS) spacecrafts 1 and 2 provides calibrated sensor data record (SDR) reflectance, radiance, and brightness temperatures for use in environment data record (EDR) products. The SDRs and EDRs are used in weather forecasting models, weather imagery and climate applications such as ocean color, sea surface temperature and active fires. The VIIRS has 22 bands covering a spectral range 0.4–12.4 μm with resolutions of 375 m and 750 m for imaging and moderate bands respectively on four focal planes. The bands are stratified into three different types based on the source of energy sensed by the bands. The reflective solar bands (RSBs) detect sunlight reflected from the Earth, thermal emissive bands (TEBs) sense emitted energy from the Earth and the day/night band (DNB) detects both solar and lunar reflected energy from the Earth. The SDR calibration uses a combination of pre-launch testing and the solar diffuser (SD), on-board calibrator blackbody (OBCBB) and space view (SV) on-orbit calibrator sources. The pre-launch testing transfers the National Institute of Standards and Technology (NIST) traceable calibration to the SD, for the RSB, and the OBCBB, for the TEB. Post-launch, the on-board calibrators track the changes in instrument response and adjust the SDR product as necessary to maintain the calibration. This paper will discuss the pre-launch radiometric calibration portion of the SDR calibration for the RSBs that includes the dynamic range, detector noise, calibration coefficients and radiometric uncertainties for JPSS-2 VIIRS.

Keywords: JPSS; VIIRS; calibration; RSB; TVAC; pre-launch; SDR; EDR

1. Introduction

The Joint Polar Satellite System (JPSS) and Suomi National Polar-orbiting Partnership (S-NPP) missions support the National Aeronautics and Space Administration (NASA) and National Oceanic and Atmospheric Administration (NOAA) weather and climate study needs. One of the main instruments on-board the JPSS and S-NPP spacecrafts is the Visible Infrared Imaging Radiometer Suite (VIIRS). It provides a calibrated and geolocated sensor data record (SDR) that feeds into 26 unique environmental data record (EDR) algorithms that compute different land, ocean, and atmospheric parameters [1–4]. These EDRs, combined with EDRs from other sensors on-board the JPSS and S-NPP spacecrafts, are used to feed weather forecasting and climate study models. There are currently three VIIRS instruments on-orbit, S-NPP, JPSS-1, and JPSS-2 that launched in November of 2022. There are two more JPSS spacecrafts after JPSS-2, with launches planned for 2027 and 2032. The VIIRS instruments are in a sun-synchronous low Earth orbit with an altitude of ~824 km and an equatorial crossing of 13:30 Greenwich Mean Time. It is a cross-scanning system with a scan range of ±56.0° covering a swath width of 3060 km. The scanning mechanism is comprised of a rotating telescope assembly (RTA) and a double-sided half-angle mirror (HAM) combination to facilitate the wide scan range with reduced straylight impacts. There are 16 moderate bands (M-bands) with each band having 16

detectors and a nadir ground resolution of 750 m. There are 5 imaging bands (I-bands) having 32 detectors each and a NADIR ground resolution of 375 m. To reduce the VIIRS ground resolution growth as it scans across the Earth, an aggregation scheme is used. The aggregation within the $\pm 32°$ scan angle region combines three scan samples to make a ground pixel, while the $-43°$ to $-32°$ and $32°$ to $43°$ scan regions combine two scan samples to make a ground pixel, and the $-56°$ to $-43°$ and $43°$ to $56°$ scan regions use a single sample to make a ground pixel. This reduces the ground pixel growth observed in heritage sensors such as Advanced Very High Resolution Radiometer (AVHRR) and Moderate Resolution Imaging Spectroradiometer (MODIS) and improves the imagery at the edges of the scan [5,6]. The day/night band (DNB) has a ground resolution of 750 m with 16 detectors but uses a more complicated aggregation scheme to maintain an almost constant resolution across scan and track directions. The 22 bands are stratified into three different types: the reflective solar bands (RSBs), the thermal emissive bands (TEBs) and the DNB. The RSBs are on the visible near infrared (VNIR) focal plane (bands M1-M7 and I1-I2), that cover a spectral range of 0.395–0.900 μm, the short-wave infrared (SWIR) FPA (bands M8-M11 and I3) having a spectral range of 1.230–2.500 μm and the day/night band (DNB) with a spectral range of 0.500–0.900 μm. The TEBs are on the mid-wave infrared (MWIR) FPA (bands M12, M13 and I4), with a spectral range of 3.700–4.130 μm, and the long-wave infrared (LWIR) FPA (bands M14-M16 and I5) with a spectral range of 8.400–12.490 μm [7].

Similar to its heritage sensor MODIS, the VIIRS SDRs provide geolocated and radiometrically calibrated top-of-atmosphere (TOA) radiance, reflectance, and brightness temperatures. The SDRs use a combination of pre-launch tests and on-orbit calibrator data to provide National Institute of Standards and Technology (NIST) traceable SDR product outputs [8]. The EDR products use diverse scenes from dark/warm oceans to bright/cold clouds that require the instrument to have a large dynamic range with adequate signal-to-noise ratio (SNR) performance throughout [9–11]. To achieve this requirement, several bands (M1-M5, M7 and M13) have dual gains for high SNRs at both dark and bright scenes without saturating. Bands M1-M5 and M7 are used for the ocean color and chlorophyl EDR that has low TOA radiances while the land and atmosphere use them for very bright radiance scenes. Band M13 is a TEB used for active fire EDRs and therefore has a large TOA brightness temperature dynamic range requirement [12]. Table 1 lists the dynamic range requirements and SNR at a typical TOA radiance for the RSBs. The DNB has three gain stages to allow day, twilight, and night-time scenes to be observed without saturation and adequate SNR. Each of the gain stages for these bands requires individual characterization to allow a seamless SDR product to be created. Each band's detectors and HAM sides are also characterized individually to reduce potential striping in the SDRs.

Table 1. VIIRS spectral, dynamic range and noise requirements for the reflective solar bands.

| Band	Spectral Range (μm)	Band Gain	Ltyp	Lmax	SNR
VNIR					
DNB	0.500–0.900	VG	0.00003	200	6
M1	0.402–0.422	High	44.9	135	352
		Low	155	615	316
M2	0.436–0.454	High	40	127	380
		Low	146	687	409
M3	0.478–0.498	High	32	107	416
		Low	123	702	414
M4	0.545–0.565	High	21	78	362
		Low	90	667	315
I1	0.600–0.680	Single	22	718	119
M5	0.662–0.682	High	10	59	242
		Low	68	651	360
M6	0.739–0.754	Single	9.6	41	199
I2	0.846–0.885	Single	25	349	150
M7	0.846–0.885	High	6.4	29	215
		Low	33.4	349	340
SWIR					
M8	1.230–1.250	Single	5.4	165	74
M9	1.371–1.386	Single	6	77.1	83
I3	1.580–1.640	Single	7.3	72.5	6
M10	1.580–1.640	Single	7.3	71.2	342
M11	2.225–2.275	Single	0.12	31.8	10

On-orbit, the SDRs use the pre-launch calibration to convert instrument digital numbers (DNs) into radiance units. The three internal calibration targets: the space view (SV), solar diffuser (SD), and the on-board calibration blackbody (OBCBB) are used to correct changes in the instrument from pre-launch to on-orbit and maintain the SDR radiometric quality [13]. The SV looks at dark space to track drifts in the instrument's offset and is also used for lunar calibration [14]. The SD tracks instrument changes in the gain of the RSBs while the OBCBB tracks gain changes for the TEBs [15,16]. Figure 1 shows an illustration of where the calibration sources are within the scan of the instrument. The Earth view is at the bottom of the image while the three calibration sources are within the instrument and are viewed when the RTA is pointing away from the Earth. The RSBs use a two-point calibration (SV offset and SD illumination) to determine the optical system's linear gain change, called the F factor, shown as

$$F = \left[\frac{H(t,\lambda)E(\lambda)\tau_{SAS}(\theta_{az},\varphi_{dec},\lambda)BRDF(\theta_{az},\varphi_{dec},\lambda)cos(\theta_{inc})}{c_0 + c_1 dn_{SD} + c_2 dn_{SD}^2} \right] \quad (1)$$

The dn_{SD} is the detector's response when viewing the illuminated SD as VIIRS crosses the south pole that is subtracted by the SV dark response when viewing cold space. This background subtraction removes the instrument's digital count offset and any dark noise drifts on a scan-by-scan basis. The c_0, c_1 and c_2 are the calibration coefficients determined during pre-launch testing. They are fixed over the mission and any change in the calibration of the sensor, away from the pre-launch performance, will show up in the *F* factor. The Thuillier solar spectral irradiance $E(\lambda)$ (λ denotes wavelength) and the bi-directional reflectance distribution function (BRDF) of the SD are used to estimate the solar radiance at the time of *F* factor measurement [17,18]. The solar attenuation screen transmission τ_{SAS} scales the estimated solar radiance and is dependent on solar azimuth (θ_{az}) and solar declination (φ_{dec}), in the spacecraft coordinate system. The BRDF also has solar azimuth and declination dependences that must be accounted for. The solar incidence angle θ_{inc} at the SD is defined as the angle between a vector pointing to the Sun and the vector normal to the SD surface. The BRDF of the SD degrades over the life of the mission due to contaminants within the surface being exposed to UV energy. This degradation is tracked using the solar diffuser stability monitor (SDSM) derived *H* factor that corrects the *F* factor in Equation (1) and is a function of time (*t*) and wavelength [15]. Figure 2 shows the geometry for the SD and SDSM during *H* factor data collection. The *H* factor in Equation (1) is determined using,

$$H = \frac{(DC_{sun}-DC_{bkg})}{(DC_{sd}-DC_{bkg})} \cdot \frac{\tau_{SAS}(\theta_{az},\varphi_{dec}) \cdot BRDF_{sd}(\theta_{az},\varphi_{dec}) \cdot sin^2(FOV_{SDSM}) \cdot cos(AOI_{sd})}{\tau_{SDSM}(\alpha_{az},\beta_{el})} \quad (2)$$

With τ_{SDSM} (the $SDSM$ screen transmittance) being a function of $SDSM$ solar azimuth α_{az} and elevation β_{el} angles. The $SDSM$ detector voltages DC_{sun}, DC_{sd}, and DC_{bkg} are from the Sun, SD and background paths, respectively. The FOV_{SDSM} is the fixed field of view of the $SDSM$ when looking at the SD, the AOI_{sd} is the angle of incidence of the $SDSM$ view relative to the SD's normal vector and $BRDF_{sd}$ is the SD reflectance at the $SDSM$ view geometry.
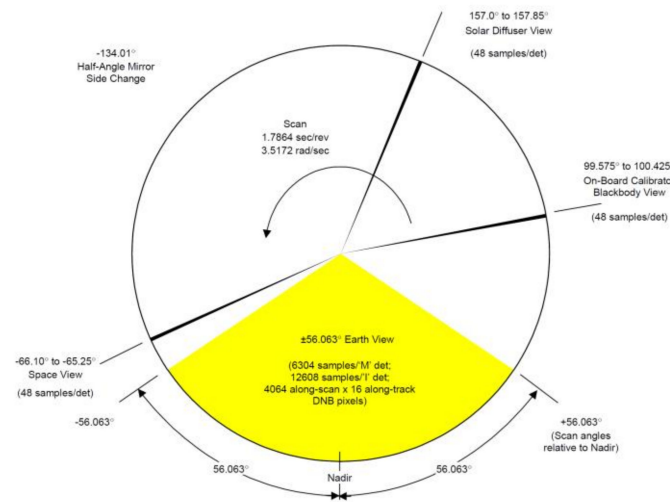
Figure 1. VIIRS scan section diagram illustrating the different collection regions and their angles during a single scan.
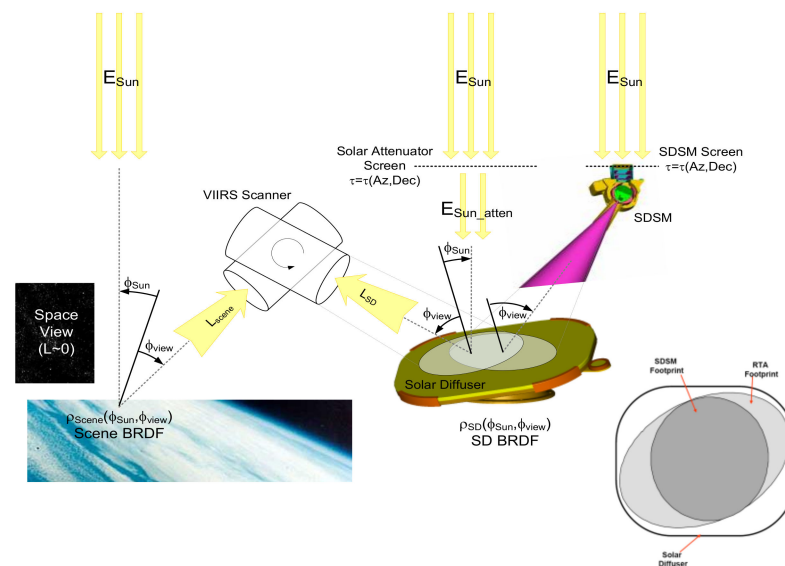
Figure 2. Diagram of the VIIRS solar diffuser calibration. This includes the VIIRS scanner that looks at the Earth and solar diffuser (*SD*) when illuminated by the Sun through an attenuation screen and the solar diffuser stability monitor (SDSM) that views the Sun through a screen and the *SD* while it is illuminated.

The Earth view TOA radiance (L_{ev}) is retrieved using the pre-launch calibration coefficients, dn_{EV} (the SV subtracted Earth view response) and the response versus scan angle (RVS) [14], that is scaled by the *F* factor as shown in

$$L_{EV} = F \frac{RVS(\theta_{SD})}{RVS(\theta_{EV})} \left(c_0 + c_1 dn_{EV} + c_2 dn_{EV}^2 \right) \tag{3}$$

The *RVS* captures the relative reflectance change of the HAM mirror as a function of scan angle and scales the calibration coefficients (c_i). The RVS is characterized pre-launch for each band, detector, and HAM side [19]. The RSBs variation in *RVS* across the scan is less than 2% with the detector-to-detector variation being within the uncertainty of the measurements. Therefore, on-orbit a detector averaged *RVS* is used for each band, unlike S-NPP and JPSS-1 VIIRS where a detector dependent *RVS* is used. Changes in the on-orbit RVS can cause striping issues in the SDRs in the cross-track direction and

detector-to-detector. The calibration coefficients c_i are used to convert the background subtracted digital numbers (dn) into a calibrated radiance using Equations (1) or (3). These calibration coefficients are determined through extensive pre-launch characterization, using NIST traceable radiance sources. The next section will describe the test and data analysis methodologies used to determine the calibration coefficients and the sensor requirements used to evaluate the VIIRS radiometric performance. The SD BRDF, attenuator screens in the SD and SDSM, and geometry factors for Equations (1) and (2) are determined pre-launch with component level measurements of each system. The SD BRDF and screen transmittance are measured at multiple azimuth and declination angles to characterize the angular dependence of their transmission and reflectance, respectively. The geometric factors used in the calibration are modeled based on specified build sizes and alignment measurements, acquired during component level integration. The solar irradiance is Thuillier 2003 and considered to be a fixed intensity throughout the on-orbit mission. The solar irradiance used for the S-NPP and JPSS missions are different and result in different SDR radiances when compared. However, the RSB SDR reflectance product is not affected by the differences in solar irradiance values. Section 3 will discuss the results of the pre-launch radiometric characterization. This includes the dynamic range, SNR, calibration coefficients and radiometric uncertainty results

2. RSB Calibration Test Methods

2.1. Spherical Integration Source and Linear Attenuation Assembly Calibrators

The response of the VIIRS RSB detectors is measured using a combination of a spherical integration source (SIS) and a linear attenuation assembly (LAA). The vendor used two different SIS setups to cover the full dynamic range of all the RSBs. The main SIS is the SIS100, due to its 100 cm diameter, that has 18, 9, and 10,200 Watt (W), 45 W and 10 W bulbs, respectively. The internal cavity of the SIS100 is coated with a diffuse material that creates a uniform and unpolarized target with a wide angular field that fills the instrument's field of view. This allows all 16 or 32 detectors to view the SIS100 simultaneously during calibration. The 37 lamps within the SIS100 allow for up to 62 different illumination levels to be used during calibration testing. These 62 levels were optimized to adequately sample all 14 RSBs throughout their dynamic ranges. This includes high, low, and single gain configurations. Bands M1–M3 low gain is not fully characterized using the SIS100 and requires a second SIS that has a higher radiance capability. This was accomplished using the three mirror collimator SIS (TMCSIS) that collimates the exit aperture of a small bright SIS and illuminates the entrance pupil of VIIRS. This allows the M1–M3 low gain to be characterized but has higher uncertainty due to the angular non-uniformity of the smaller SIS and the mirrors used to collimate that energy. The radiance spectral profile of the SIS100 differs with respect to the on-orbit radiance that uses reflected solar irradiance as its source. Figure 3 shows a normalized radiance profile from the SIS100 (orange curve) where the peak response is around ~0.800 μm and the normalized on-orbit solar irradiance that peaks at ~0.450 μm. This is important for bands with out-of-band (OOB) spectral response and bands such as M1 where the slope of the two source profiles is large. S-NPP VIIRS has several VNIR bands with OOB spectral features that affected the pre-launch calibration uncertainty [20]. However, the JPSS instruments do not have these OOB features and therefore are not similarly impacted by the source spectral differences. The differences in the pre-launch and on-orbit sources are captured in the radiometric uncertainty analysis shown in Section 3.
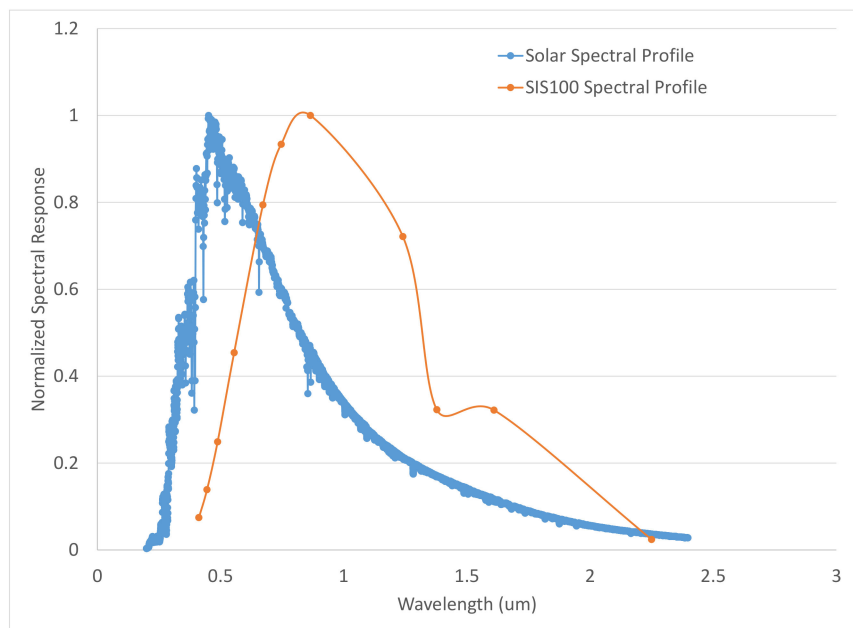
Figure 3. A comparison of the on-orbit solar spectral irradiance profile and the SIS100 radiance profile. The OOB Relative Spectral Response (RSR) contributions are not weighted the same in on-orbit and prelaunch applications.

The NIST traceability of the SIS100 calibration is performed using an ASD$^{\circledR}$ spectrometer for each lamp used in the pre-launch test [21]. The uncertainty of the SIS100 calibration ranges between 1–5% due to lamp stability and drift between NIST calibration and prelaunch VIIRS testing and is larger than the 0.3% calibration coefficient characterization uncertainty requirement. To mitigate the SIS100 lamp's long-term instability, the LAA is used to take two measurements, LAA in and LAA out, at each SIS lamp level within a few minutes of each other. This requires the SIS100 to be stable for a few minutes instead of hours or days. Equations (4) and (5) represent the 2nd order polynomial equations with the LAA out (Equation (4)) and the LAA in (Equation (5)). The dn_{out} and dn_{in} are the VIIRS detector's response, after background subtraction from the space view, for the LAA out and in, respectively. The τ_{LAA} is the transmittance of the LAA pinhole screen and the c_0, c_1 and c_2 are the calibration coefficients. When

$$L_{SIS100} = c_0 + c_1 dn_{out} + c_2 dn_{out}^2 \tag{4}$$

and

$$L_{SIS100} = \frac{\left(c_0 + c_1 dn_{in} + c_2 dn_{in}^2\right)}{\tau_{LAA}} \tag{5}$$

are combined by substituting for LSIS100, Equation (6) is formed, that removes the linear coefficient c_1 and the L_{SIS100} and has the τ_{LAA} transmittance and the relative offset $\left(\frac{c_0}{c_1}\right)$ and 2nd order term $\left(\frac{c_2}{c_1}\right)$ with respect to the linear term. It can also be used with the TMCSIS measurements since it is independent of the source radiance value.

$$dn_{in} = (\tau_{LAA} - 1)\frac{c_0}{c_1} + \tau_{LAA} dn_{out} + \frac{c_2}{c_1}\left(\tau_{LAA} dn_{out}^2 - dn_{in}^2\right) \tag{6}$$

allows the shape of the detector response to be determined independent of the SIS100 radiance and is relative to the linear term c_1. This removes the lamp calibration uncertainty from the fit and minimizes source drift effects because of the close temporal proximity of the in and out measurements. A regression fit of the pre-launch measurement data is performed using Equation (6) to determine the LAA transmittance and coefficient ratios for

each band, detector, HAM side and gain state. The c_1 is determined using the computed calibration coefficient ratios and NIST traceable SIS100 radiances, as shown in

$$c_1 = \frac{L_{SIS100}}{\frac{c_0}{c_1} + dn_{out} + \frac{c_2}{c_1} dn_{out}^2} \tag{7}$$

while the SIS100 radiance can add an error bias of 1–5%, the on-orbit SD calibration will remove this bias. The shape of the detector response is well characterized by the calibration coefficient ratios, and the bias is removed on-orbit.

2.2. JPSS-2 VIIRS Testing and Analysis Methodology

JPSS-2 VIIRS pre-launch radiometric testing was performed during ambient and thermal vacuum (TVAC) phases. The ambient test phase (~295 K room temperature) is used to check the health of the detectors, dynamic range, noise, and dual gain switching for both electronics sides A and B. Results from ambient testing allow adjustments or modifications to the hardware where non-compliant behavior was observed. TVAC testing measures the dynamic range, noise, gain switching but also characterizes the detector response at three temperature plateaus: cold (−20 °C), nominal (−5 °C) and hot (10 °C). The results of the TVAC radiometric performance are compared to the instrument specification and used in on-orbit look-up tables (LUTs). The focus of this paper is on the TVAC measurements and their performance relative to the specifications.

The VIIRS radiometric tests are performed in two different configurations: steady state temperature and dynamic temperature measurements. The steady state measurements are at each plateau and characterize the instrument calibration coefficients but also measure the medium-term stability of the detector response. The dynamic temperature tests capture the detector's gain change with respect to instrument temperature that are taken during TVAC temperature plateau transitions.

The steady state tests rely on the SIS100 and TMCSIS as the sources and cover the dynamic range, SNR, calibration coefficients and stability of the RSB detectors. The dynamic range analysis uses a DN average of approximately 30 M-band samples and 50 scans when viewing the SIS100 with the DC offset subtracted using the SV sector DNs to obtain what is called dn. The dns are computed for every RSB detector, HAM side, gain (using fixed high or low) and sub-sample (for I-bands only) for all SIS100 or TMCSIS lamp levels. A linear fit of SIS radiance versus unsaturated RSB detector dns is performed. The maximum unsaturated dn response of the detector is then used in the linear fit to assess the maximum measurable radiance and is compared to the specification in Table 1.

The SNR is computed using the same data as the dynamic range calculation. The SNR computation for the VIIRS detectors is

$$SNR = \left\langle \frac{\langle dn\,(Sample)\rangle_{scan}}{\langle \sigma\,(Sample)\rangle_{scan}} \right\rangle_{sample} \tag{8}$$

The *dns* are averaged over the 50 scans for each of the approximated 30 M-band samples with the standard deviation (σ) also computed. The ratio of the dns with σ is the SNR and is computed for each RSB detector, HAM side, gain and sub-frame (I-bands only), SIS level and sample. The SNRs are then averaged over samples to get the final value. This averaging technique reduces the impact of SIS spatial non-uniformity on the σ values. The SNR versus SIS radiance is modeled with

$$SNR = \frac{L_{SIS100}}{\sqrt{a_0 + a_1 L_{SIS100} + a_2 L_{SIS100}^2}} \tag{9}$$

where the a coefficients model the dark, read and shot noise of the detector. The SNR at the RSB's specified L_{typ} is interpolated using Equation (9) for each detector, HAM side, gain and sub-sample (for I-bands only).

The calibration coefficients use the same averaged dns and SIS radiance from the dynamic range analysis to perform the regression fit described in Equation (6) and as an input into Equation (7). The residuals of those fits are evaluated against the 0.3% error budget allocation to assess characterization quality. The 2-sigma error bars are computed to assess the uncertainty in the knowledge of each coefficient in Equation (6). This guides the on-orbit LUT development where the τ variation across detector or TVAC plateau or the $\frac{c_0}{c_1}$ uncertainty straddling zero can be evaluated. The linearity, while not a requirement anymore, is still looked at to better understand possible on-orbit calibration challenges as low or high radiance scenes.

The dynamic temperature test uses the SIS100 with a fixed lamp level of 4200 W lamps during the instrument transition from TVAC cold-to-nominal and nominal-to-hot plateaus. The detector's response sensitivity to opto-mechanical module (OMM) and electronics module (EM) temperatures is characterized individually. This is performed by transiting the optics and electronics separately in TVAC using unique thermal panels within the TVAC chamber. The thermal gain sensitivity is important for on-orbit calibration purposes where the instrument temperature can vary by several degrees between calibrations at the South Pole. With the calibration coefficient characterization in a thermally steady state environment, the temperature sensitivity in the coefficients is not captured. This transition gain sensitivity data is combined with the steady state calibration coefficients during on-orbit LUT development to mitigate the temperature effect as much as possible. The next section will show radiometric calibration results from the JPSS-2 VIIRS TVAC testing as well as compare the performance with S-NPP and JPSS-1 VIIRS

3. Results

3.1. Dynamic Range

The dynamic range is shown in Table 2 for JPSS-2 (top) and -1 (bottom) and meets or exceeds the requirements listed in Table 1 for all bands except M8. There are three columns for each band and gain configuration; measured saturation radiance, saturation requirement and the ratio of measured with requirement. The requirements margins are larger for JPSS-2 than −1 and are above 10% with the exclusion of bands M6 and M8. An example of the dynamic range in auto gain mode is shown in Figure 4 for M4 HAM A. The vertical red lines correspond to the Lmax for high (left) and low (right) gain, respectively, and the points show how each detector's response (y-axis) changes with SIS100 radiance (x-axis). Band M4 saturation occurs at ~870 W/m^2/sr/μm and is well past the 667 W/m^2/sr/μm Lmax requirement. The points past 870 W/m^2/sr/μm on the x-axis are flat where the digital-to-analog converter (ADC) is saturated. Figure 5 shows the dynamic range for band I3 where saturation occurs at ~105 W/m^2/sr/μm before the dns begin to rollover. This is due to the focal plane electronics, or read out integrated circuit (ROIC), saturating before the ADC. Bands I3 and M6 have this saturation behavior that affects the on-orbit SDR calibration. Bright targets such as clouds and glint can cause deep saturation that appears to be a lower radiance in the SDR product due to the reduced saturated dns recorded by the instrument. This rollover effect is present in S-NPP and JPSS-1 and has an SDR algorithm flagging to mitigate its impact on EDRs.

Table 2. Measured dynamic range performance for the reflective solar bands. The top portion is for JPSS-2 and band M8 fails the instrument specification. The bottom portion is for JPSS-1 where several bands failed to meet the instrument requirements.

JPSS-2	Single Gain			High Gain			Low Gain		
	L_sat	L_max	L_sat/L_max	L_sat	L_max	L_sat/L_max	L_sat	L_max	L_sat/L_max
I1	1019	718	1.42	-	-	-	-	-	-
I2	421	349	1.21	-	-	-	-	-	-
I3	106	72.5	1.46	-	-	-	-	-	-
M1	-	-	-	168	135	1.25	765	615	1.24
M2	-	-	-	155	127	1.22	921	687	1.34
M3	-	-	-	121	107	1.13	1000	702	1.43
M4	-	-	-	99.8	78	1.28	871	667	1.31
M5	-	-	-	74.5	59	1.26	1068	651	1.64
M6	46.3	41	1.13	-	-	-	-	-	-
M7	-	-	-	34.9	29	1.20	417	349	1.20
M8	156	165	0.95	-	-	-	-	-	-
M9	87.5	77.1	1.13	-	-	-	-	-	-
M10	105	71.2	1.47	-	-	-	-	-	-
M11	52.5	31.8	1.65	-	-	-	-	-	-
JPSS-1	Single Gain			High Gain			Low Gain		
	L_sat	L_max	L_sat/L_max	L_sat	L_max	L_sat/L_max	L_sat	L_max	L_sat/L_max
I1	772	718	1.08	-	-	-	-	-	-
I2	401	349	1.15	-	-	-	-	-	-
I3	65.2	72.5	0.90	-	-	-	-	-	-
M1	-	-	-	164	135	1.21	710	615	1.15
M2	-	-	-	173	127	1.36	797	687	1.16
M3	-	-	-	144	107	1.35	851	702	1.21
M4	-	-	-	113	78	1.44	863	667	1.29
M5	–	–	–	76.5	59	1.30	733	651	1.13
M6	46.8	41	1.14	–	–	–	–	–	–
M7	–	–	–	38.1	29	1.31	414	349	1.19
M8	115	165	0.69	–	–	–	–	–	–
M9	72.1	77.1	0.93	–	–	–	–	–	–
M10	77.0	71.2	1.08	–	–	–	–	–	–
M11	33.5	31.8	1.05	–	–	–	–	–	–
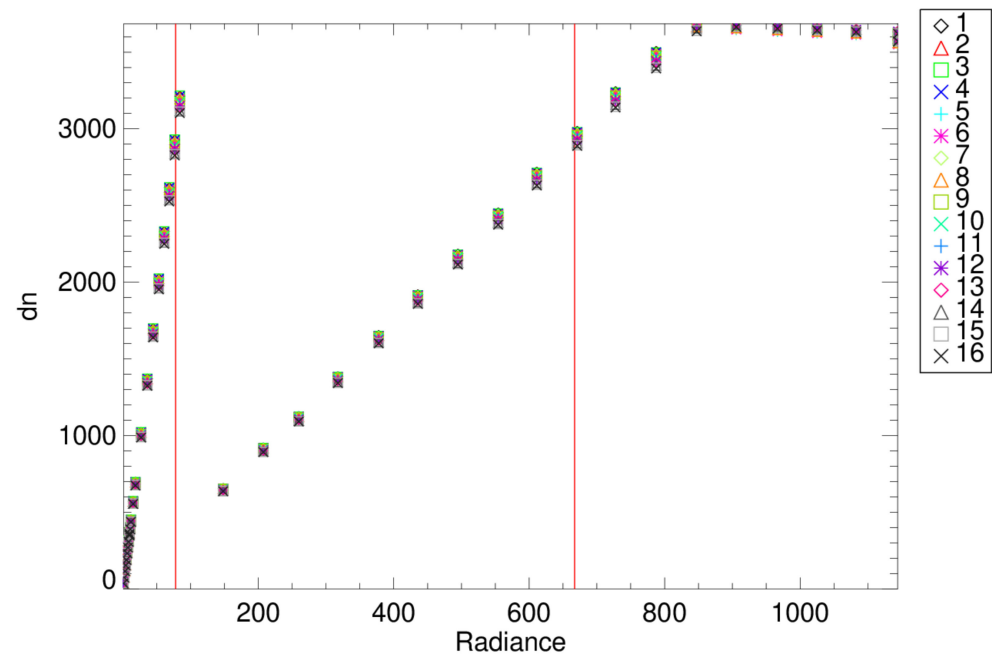
Figure 4. Band M4 dynamic range measurements for all detectors, legend in the upper right, for HAM side A. The points to the left of the first vertical line are high gain measurements. The band switches to low gain after a radiance of ~100. The first and second vertical red lines are for high and low gain Lmax, respectively. The y-axis is offset subtracted VIIRS response, and the x-axis is the SIS100 radiance during the measurement.
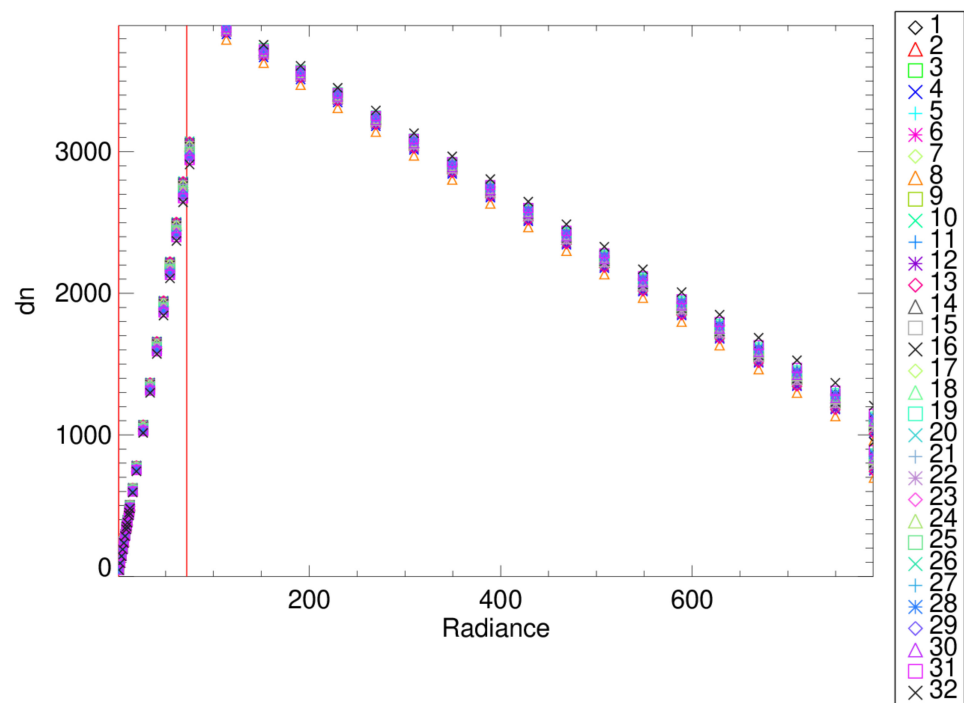
Figure 5. Band I3 dynamic range measurements for all detectors, legend in the upper right, for HAM side A. The y-axis is offset subtracted VIIRS response, and the x-axis is the SIS100 radiance during the measurement. The second vertical red line corresponds to Lmax. The rollover in the response is due to saturation of the focal plane electronics. This causes two unique radiance levels to produce the same VIIRS digital number.

3.2. Dual Gain Switch

The dual gain switch analysis verified the transition from high to low gain was within the specified radiance range. Figure 4 shows an example of the auto gain transition for band M4. A more accurate assessment of the gain switching was performed using the gradual increase/decrease in signal as the instrument detectors scan on/off of the SIS100 profile. This provides a higher fidelity assessment of the gain switch point relative to the information in Figure 4. The dn or radiance at the high-to-low gain transition can be calculated and compared to the specification. Table 3 lists the gain transition for the JPSS-2 RSBs and the required transition region specified. The JPSS-1 results are also listed to show the consistency between instrument builds.

Table 3. JPSS-2 VIIRS dual gain switching for all the RSBs. The dual gain switching for band M1 could not be measured for most configurations due to the limited maximum radiance output of the SIS100.

JPSS-2										
						L at Transition			Ratio of Switch with Requirement		
Band	E Side	HAM	Lmin Switch Point	Lmax Switch Point		Temperature Plateau			Temperature Plateau		
					Cold	Nominal	Hot	Cold	Nominal	Hot
M1	A	A	135	202.5	NA	NA	NA	NA	NA	NA
M1	A	B	135	202.5	NA	NA	NA	NA	NA	NA
M2	A	A	127	190.5	155.6	156.8	158.1	1.22	1.23	1.25
M2	A	B	127	190.5	155.2	156.4	157.7	1.22	1.23	1.24
M3	A	A	107	160.5	112.5	113.8	114.3	1.05	1.06	1.07
M3	A	B	107	160.5	112.3	113.6	114.2	1.05	1.06	1.07
M4	A	A	78	117	86.5	87.2	87.9	1.11	1.12	1.13
M4	A	B	78	117	86.5	87.2	87.8	1.11	1.12	1.13
M5	A	A	59	88.5	67.6	68.4	69.3	1.15	1.16	1.17
M5	A	B	59	88.5	67.7	68.4	69.3	1.15	1.16	1.17
M7	A	A	29	43.5	32.3	32.7	33.1	1.11	1.13	1.14
M7	A	B	29	43.5	32.3	32.7	33.1	1.11	1.13	1.14
M1	B	A	135	202.5	NA	NA	184.4	NA	NA	1.37
M1	B	B	135	202.5	NA	NA	183.6	NA	NA	1.36
M2	B	A	127	190.5	155.7	156.8	157.7	1.23	1.23	1.24
M2	B	B	127	190.5	155.4	156.4	157.6	1.22	1.23	1.24
M3	B	A	107	160.5	112.3	113.7	114.5	1.05	1.06	1.07
M3	B	B	107	160.5	112.3	113.6	114.5	1.05	1.06	1.07
M4	B	A	78	117	86.6	87.3	87.6	1.11	1.12	1.12
M4	B	B	78	117	86.4	87.2	87.6	1.11	1.12	1.12
M5	B	A	59	88.5	67.6	68.4	69.3	1.15	1.16	1.17
M5	B	B	59	88.5	67.6	68.4	69.2	1.15	1.16	1.17
M7	B	A	29	43.5	32.3	32.7	33.0	1.11	1.13	1.14
M7	B	B	29	43.5	32.3	32.7	33.0	1.11	1.13	1.14

Table 3. *Cont.*

JPSS-1

| Band	E Side	HAM	Lmin Switch Point	Lmax Switch Point	L at Transition Temperature Plateau			Ratio of Switch with Requirement Temperature Plateau		
					Cold	Nominal	Hot	Cold	Nominal	Hot
M1	A	A	135	202.5	167.2	155.5	158.9	1.24	1.15	1.18
M1	A	B	135	202.5	169.3	158.0	161.3	1.25	1.17	1.19
M2	A	A	127	190.5	161.5	153.0	156.3	1.27	1.21	1.23
M2	A	B	127	190.5	162.6	154.0	157.4	1.28	1.21	1.24
M3	A	A	107	160.5	122.2	115.3	118.4	1.14	1.08	1.11
M3	A	B	107	160.5	122.5	115.5	118.6	1.14	1.08	1.11
M4	A	A	78	117	98.3	92.5	95.4	1.26	1.19	1.22
M4	A	B	78	117	98.2	92.4	95.3	1.26	1.18	1.22
M5	A	A	59	88.5	66.9	62.3	65.1	1.13	1.06	1.10
M5	A	B	59	88.5	66.6	62.0	64.8	1.13	1.05	1.10
M7	A	A	29	43.5	33.4	30.7	32.5	1.15	1.06	1.12
M7	A	B	29	43.5	33.5	30.8	32.6	1.16	1.06	1.12
M1	B	A	135	202.5	169.3	157.8	165.8	1.25	1.17	1.23
M1	B	B	135	202.5	170.0	160.2	168.6	1.26	1.19	1.25
M2	B	A	127	190.5	163.7	155.0	160.7	1.29	1.22	1.27
M2	B	B	127	190.5	164.6	156.1	161.7	1.30	1.23	1.27
M3	B	A	107	160.5	123.9	117.0	121.1	1.16	1.09	1.13
M3	B	B	107	160.5	124.1	117.1	121.3	1.16	1.09	1.13
M4	B	A	78	117	99.5	93.8	97.1	1.28	1.20	1.25
M4	B	B	78	117	99.2	93.6	97.1	1.27	1.20	1.25
M5	B	A	59	88.5	67.9	63.9	66.3	1.15	1.08	1.12
M5	B	B	59	88.5	67.5	63.7	66.0	1.14	1.08	1.12
M7	B	A	29	43.5	33.7	32.0	33.1	1.16	1.10	1.14
M7	B	B	29	43.5	33.6	32.0	33.1	1.16	1.10	1.14

3.3. SNR Results

The median SNRs at Ltyp for all the RSBs are listed in Table 4 for JPSS-2 (top table) and JPSS-1 (lower table). The bands are stratified by single (left), high (middle), and low (right) gain configurations. Each gain configuration has three columns, the first is the measured SNR for that band, the middle is the instrument requirement and the last is the ratio of measured and requirement. The JPSS-2 RSBs meet the SNR requirement for all bands and detectors. They are marginally lower for most bands (except bands M3 and M4) than the JPSS-1 values but still far exceed the instrument requirements. Not listed in the Table 4 is the JPSS-1 band I3 detector 4 (instrument order) that is a bad detector. There are no noisy or inoperable detectors identified in pre-launch testing for JPSS-2 VIIRS. The detector quantization effects that are present on S-NPP and JPSS-1 are also present on JPSS-2 VIIRS. The quantization appears at low radiance levels for single gain bands I1 and M10 and for the low gain in bands M1–M5 and M7. The low gain quantization is present in the pre-launch test data due to it being in a fixed low gain setting. On-orbit, where the instrument will be in auto gain mode, the quantization may not be present and depends on the gain switch point of the band. Figures 6 and 7 show the SNR versus SIS100 radiance for bands M8 and M10. The symbols correspond to the detectors and only show HAM A results. The vertical red lines are Lmin (left), Ltyp (middle) and Lmax (right). These detectors are dominated by photon shot noise throughout most of the SNRs but at the low radiance region band M10 has quantization features that are not present in the M8 plot.

The quantization causes higher SNRs due to the DNs being stuck within one or two DN bins (or values) because the bins are larger than the noise of the detector. This causes the standard deviation of the DNs to be very small and increase the SNR value. The vertical red lines show that the quantization in band M10 is within the specified dynamic range and even present at a typical scene radiance for some detectors. These effects are not included in the SNR Table 4 but are part of the fit residuals in the calibration coefficient uncertainty in the next section.

Table 4. Signal-to-noise ratio (SNR) results for the VIIRS reflective solar bands. The SNR, SNR requirement and the ratio of the two are shown here. The top portion is for JPSS-2 and the bottom JPSS-1 for comparison purposes.

| | **JPSS-2** | | | | | | | | |
| | **Single Gain** | | | **High Gain** | | | **Low Gain** | | |
	Average SNR	**Spec**	**SNR/Spec**	**Average SNR**	**Spec**	**SNR/Spec**	**Average SNR**	**Spec**	**SNR/Spec**
I1	213	119	1.79	-	-	-	-	-	-
I2	259	150	1.72	-	-	-	-	-	-
I3	156	6	26.1	-	-	-	-	-	-
M1	-	-	-	566	352	1.61	834	155	5.38
M2	-	-	-	547	380	1.44	946	146	6.48
M3	-	-	-	697	416	1.67	959	123	7.80
M4	-	-	-	558	362	1.54	893	90	9.92
M5	-	-	-	315	242	1.30	737	68	10.8
M6	373	41	9.104	-	-	-	-	-	-
M7	-	-	-	514	215	2.39	885	33.4	26.5
M8	257	165	1.56	-	-	-	-	-	-
M9	146	77.1	1.90	-	-	-	-	-	-
M10	625	71.2	8.79	-	-	-	-	-	-
M11	63.5	31.8	2.00	-	-	-	-	-	-
	JPSS-1								
	Single Gain			**High Gain**			**Low Gain**		
	Average SNR	**Spec**	**SNR/Spec**	**Average SNR**	**Spec**	**SNR/Spec**	**Average SNR**	**Spec**	**SNR/Spec**
I1	307	119	2.58	-	-	-	-	-	-
I2	278	150	1.86	-	-	-	-	-	-
I3	187	6	31.1	-	-	-	-	-	-
M1	-	-	-	629	352	1.79	878	155	5.67
M2	-	-	-	568	380	1.49	1009	146	6.91
M3	-	-	-	692	416	1.66	1156	123	9.40
M4	-	-	-	542	362	1.50	962	90	10.7
M5	-	-	-	377	242	1.56	928	68	13.7
M6	424	41	10.4	-	-	-	-	-	-
M7	-	-	-	543	215	2.52	1148	33.4	34.4
M8	390	165	2.37	-	-	-	-	-	-
M9	303	77.1	3.93	-	-	-	-	-	-
M10	827	71.2	11.6	-	-	-	-	-	-
M11	69.7	31.8	2.19	-	-	-	-	-	-
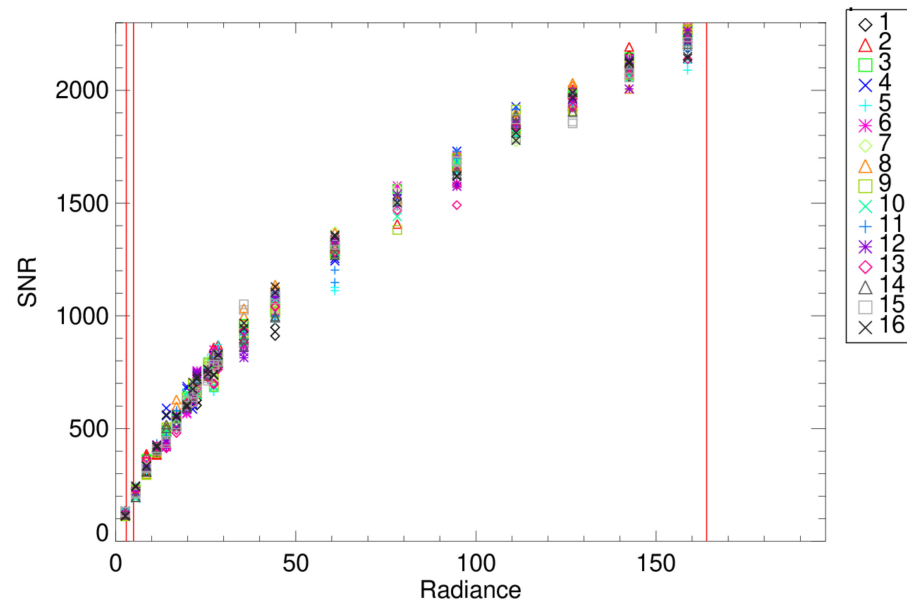
Figure 6. The signal-to-noise ratio (SNR) of band M8 for all detectors (colored symbols) as a function of SIS100 radiance (W/m^2/μm/sr). The three vertical red lines are for Lmin (left), Ltyp (middle) and Lmax (right).
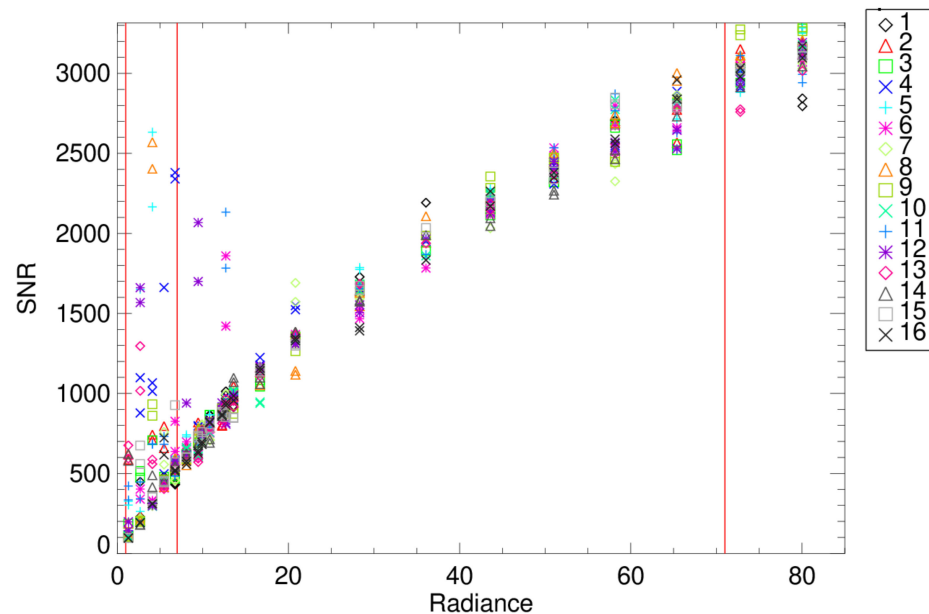

Figure 7. The signal-to-noise ratio (SNR) of band M10 for all detectors (colored symbols) as a function of SIS100 radiance (W/m^2/μm/sr). The three vertical red lines are for Lmin (left), Ltyp (middle) and Lmax (right). Digital quantization noise is impacting the low signal levels in the bottom left corner of the image.

3.4. Detector Response Characterization

The pre-launch calibration coefficients for on-orbit use in the SDR algorithm use the radiometric characterization methodology discussed in Section 2. Each band, detector, HAM side, and gain have a set of coefficients computed for each TVAC temperature plateau and primary/redundant electronics side. There are also three FPA temperatures for the SWIR bands at nominal plateau that are not discussed here. Figure 8 shows an example of the regression coefficients τ, $\frac{c_0}{c_1}$ and $\frac{c_2}{c_1}$ from the SIS100 measurements for band M1 high gain for all TVAC temperature plateaus electronic sides. The first column corresponds to the tau coefficients as a function of detector with the different colors corresponding

to the six-temperature plateau and electronic side combinations, the second column the $\frac{c_0}{c_1}$ and the third the $\frac{c_2}{c_1}$. The rows show the results for the different HAM sides with the first being HAM A and the second HAM B. The whiskers on the points represent the two-sigma uncertainty in the coefficients using the covariance matrix of the least squares regression shown in Equation (6). There is variation in the τ (column 1) over detector and TVAC plateau that has a reverse correlation with the $\frac{c_2}{c_1}$ (column 2). For example, the black diamonds for TVAC cold plateau electronics side A are higher than the rest in the τ but lower than the rest in the $\frac{c_2}{c_1}$. In an ideal measurement the τ should be a constant number over detector and temperature plateau due to it being a simple pin-hole screen placed between the SIS and the instrument. As seen in Figure 8, the τ is changing over detector and temperature. This indicates the τ in the regression fit of Equation (6) is absorbing errors in the measurements. This then causes the $\frac{c_2}{c_1}$ to balance in the opposite direction. The τ and $\frac{c_2}{c_1}$ correlation are even more evident in the band M1 low gain measurements where the less uniform TMCSIS is used.
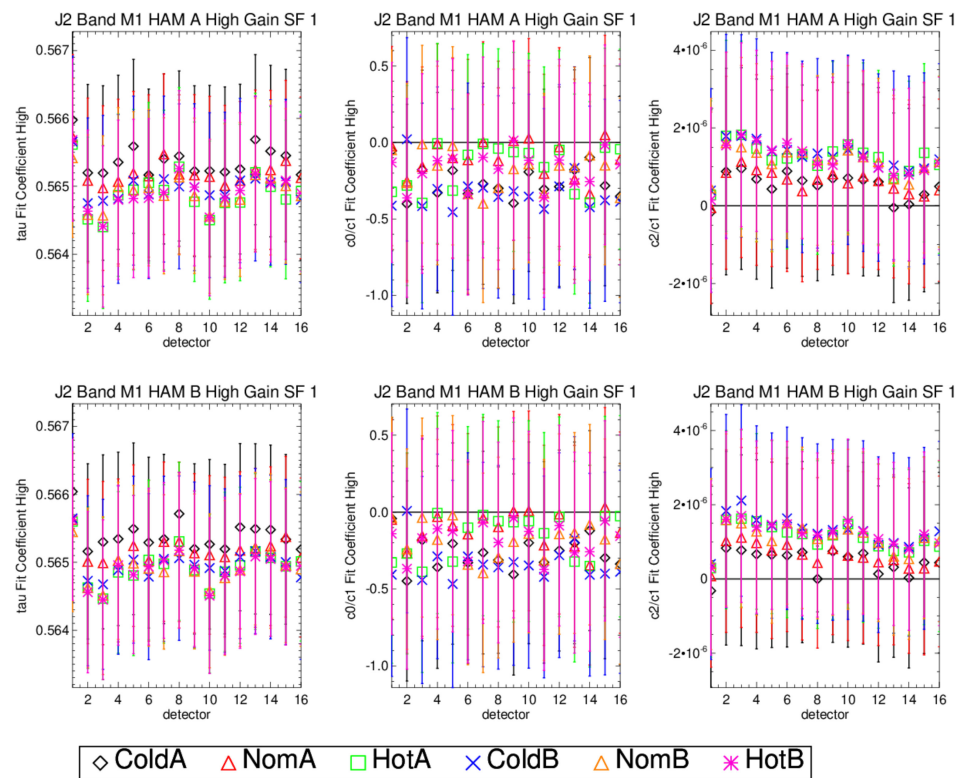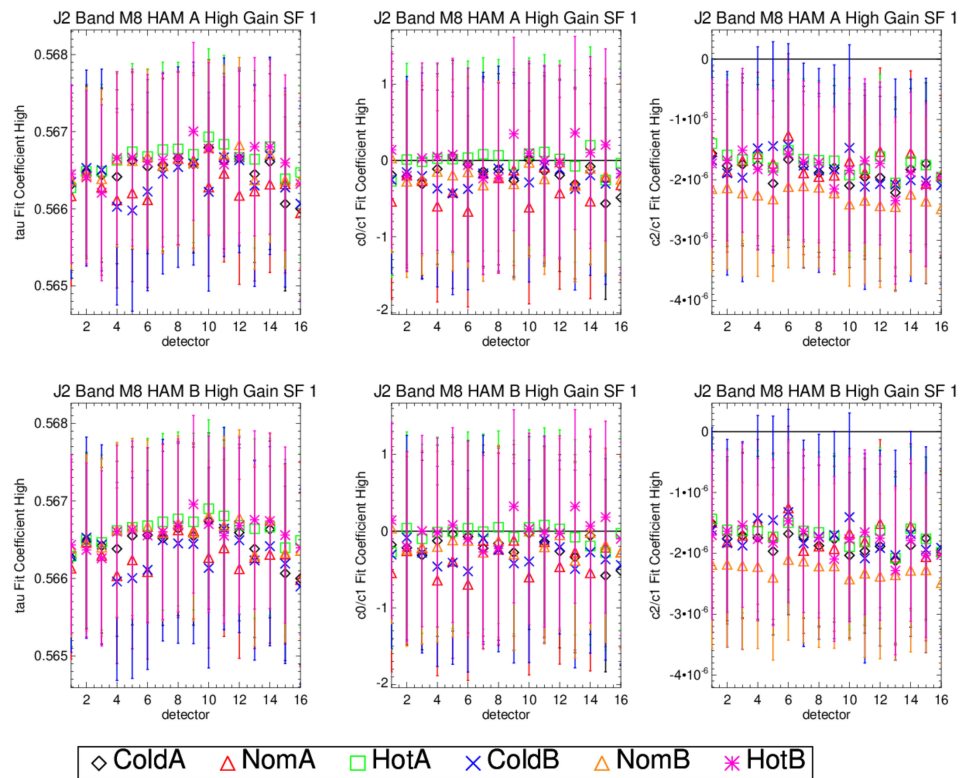

Figure 8. Band M1 high gain fit coefficients for all detectors (x-axis) and TVAC/electronics configurations (colors and symbols). The columns are tau, $\frac{c_0}{c_1}$, $\frac{c_2}{c_1}$, respectively. The rows are HAM A and B, respectively.

Figure 9 shows the band M1 regression coefficient fits for τ, $\frac{c_0}{c_1}$ and $\frac{c_2}{c_1}$ from the TMCSIS measurements for low gain, all TVAC temperature plateaus, and electronic sides. The τ has more variation than the high gain measurement and therefore the $\frac{c_2}{c_1}$ does as well. The $\frac{c_0}{c_1}$ does not have a clear relationship with the other two coefficients and captures offset errors while the other two are capturing non-linear shape errors. The 2-sigma uncertainty whiskers indicate that band M1 high and low gains could set the $\frac{c_0}{c_1}$ and $\frac{c_2}{c_1}$ to zero due to the zero line being within the uncertainty of the measurements. This indicates this band is very linear and the non-linear term is within the uncertainty of the measurements. Figure 10 shows the τ, $\frac{c_0}{c_1}$ and $\frac{c_2}{c_1}$ regression coefficients for band M8. Here the $\frac{c_2}{c_1}$ 2-sigma error bars do not cross the zero line and indicate there is a non-linear behavior that should be accounted for in the calibration coefficients on-orbit.
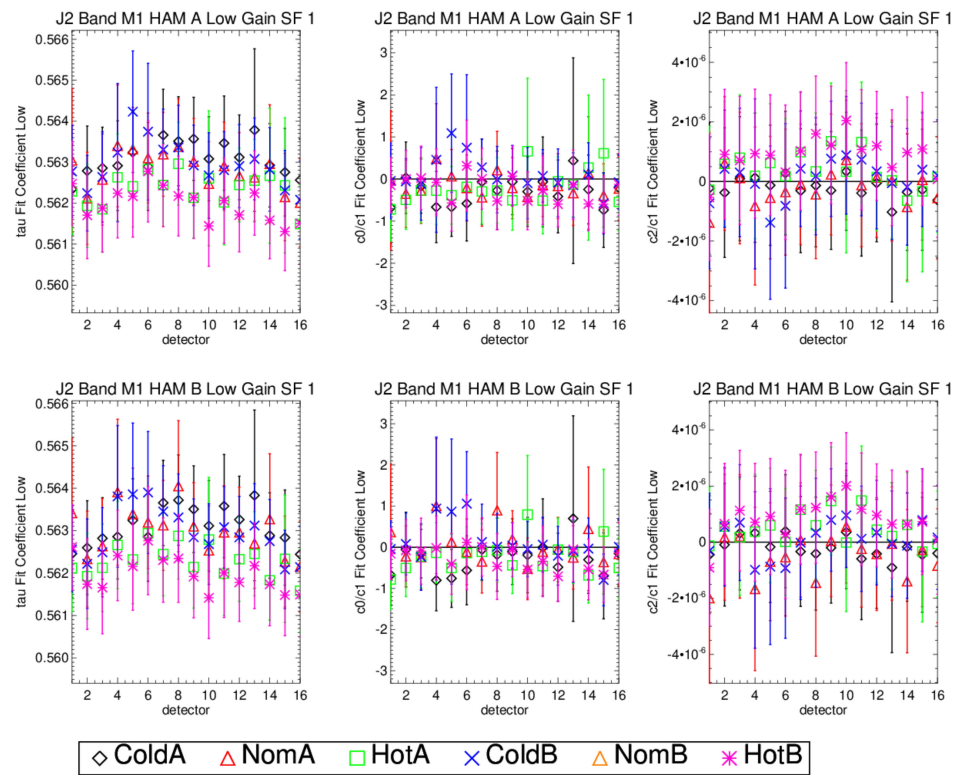
Figure 9. Band M1 low gain fit coefficients for all detectors (x-axis) and TVAC/electronics configurations (colors and symbols). The columns are tau, $\frac{c_0}{c_1}$, $\frac{c_2}{c_1}$, respectively. The rows are HAM A and B, respectively.


Figure 10. Band M8 fit coefficients for all detectors (x-axis) and TVAC/electronics configurations (colors and symbols). The columns are tau, $\frac{c_0}{c_1}$, $\frac{c_2}{c_1}$, respectively. The rows are HAM A and B, respectively.

The τ, $\frac{c_0}{c_1}$ and $\frac{c_2}{c_1}$ regression coefficients are shown in Figures 11–13, respectively, for all RSBs and detectors, HAM A, nominal B-side electronics. The upper left box shows I-bands I1–I3, upper right high/single gain VNIR M-bands M1–M7, lower right low gain VNIR M-bands M1–M5 and M7, and the lower left shows the SWIR M-bands M8–M11. The τ values in Figure 11 are consistent at around 0.566 for the I-bands, SWIR bands and the high gain VNIR bands. These bands all use the SIS100 during characterization. The VNIR low gain bands in the bottom right plot show two different groupings. The SIS100 data for bands M4, M5, and M7 are near 0.566 while the TMCSIS values for M1–M3 are near 0.563 and have more variability across detector. Figure 12 shows the $\frac{c_0}{c_1}$ with all the bands being near the zero line except for bands M2 and M3 low gain showing some spikes for a few detectors. The $\frac{c_2}{c_1}$ in Figure 13 shows the non-linear behavior does vary between bands. The 2-sigma uncertainty bars are not shown here, but they would be used to determine whether the coefficients straddle the zero line and could be considered statistically significant. As shown in Figure 10, the SWIR band M8 $\frac{c_2}{c_1}$ term uncertainties do lie outside the zero line and the other SWIR bands show similar non-linear characteristics. The dual gain M-bands show consistent non-linear behavior between high and low configurations even when the TMCSIS and SIS100 are used for each of those measurements, respectively. This indicates that the attenuator method reduces the SIS non-uniformity and instability uncertainties on the response shape characterization. Table 5 lists the c_1 coefficients for each band, gain state and TVAC temperature plateau using the calibration coefficient ratios and SIS100 radiance, as shown in Equation (7). While the non-linear response of the detectors should be consistent over TVAC temperature plateaus, the c_1 response term is expected to change with focal plane temperature. The c_1 correlates with instrument temperature with both increasing in value from cold-to-hot plateaus. The SWIR band c_1 change is much smaller (0.5–0.85%) than the VNIR bands (0.85–4%). This is expected since the SWIR focal plane is temperature controlled and the gain change is most likely due to EM temperature change while the VNIR has both OMM and EM sensitivities. Band M9 shows a large variation due to changes in the water vapor between plateau measurements. This effect is removed and not included in the on-orbit LUTs. JPSS-1 VIIRS has a nonlinear response behavior in the SWIR bands that is not present in S-NPP or JPSS-2 VIIRS. This requires JPSS-1 VIIRS to have a 3rd order polynomial term in its on-orbit calibration coefficient LUT to improve low radiance radiometric performance [22]. The JPSS-2 VIIRS LUTs are 2nd order polynomial fits, as with S-NPP.

### 3.5. Response Sensitivity to Instrument Temperature

The response change versus EM or focal plane temperature is measured during the transitions between TVAC plateaus. The rate of change in the response versus the delta temperature of either the EM or focal plane change is computed and is a correction to the calibration coefficients. With on-orbit calibration measurements only at the South Pole, intra-orbital temperature corrections of the calibration coefficients are required. Figures 14 and 15 show an example of the band M1 response change (δL) as a function of temperature change (δT) for the EM and OMM, respectively, during the transition between cold and nominal plateaus. Each symbol represents a measurement captured during the plateau transition and each color corresponds to a detector within band M1. The fit lines in the figures are used to model the temperature sensitivities for requirements assessment and on-orbit look-up table (LUT) creation. The focal plane sensitivity for band M1 is on the order of 0.0015 W/m^2/sr/μm per 1 K change in temperature. The on-orbit variations within one orbit are in the order of 2 K. This indicates the impact of the response sensitivity to temperature is around 0.0030 W/m^2/sr/μm or less within an orbit. The band M1 response sensitivity to the EM is around -0.0051 W/m^2/sr/μm over a 1 K range. Orbital EM temperature variation is expected to be within ~0.5 K, making the temperature sensitivity of the response to the EM temperature almost negligible. Table 6 lists the temperature sensitivities for all the bands for both the EM and OMM.
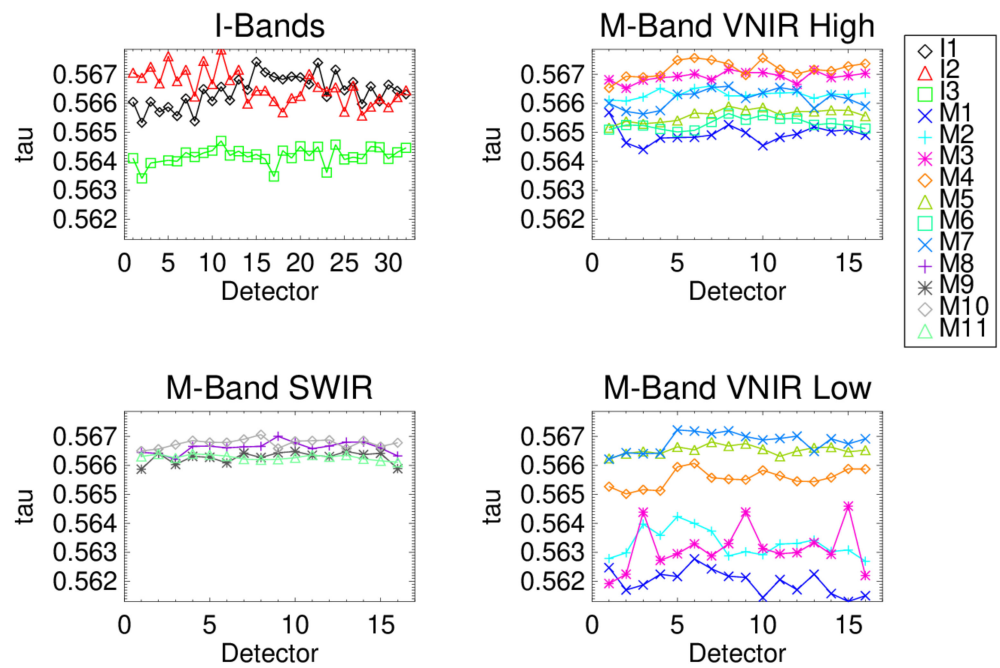
Figure 11. Comparison of the tau coefficient for all RSBs at nominal TVAC plateau. The upper left are the I-bands, upper right high gain VNIR M-bands, lower left the SWIR M-bands, and the lower right the low gain VNIR M-bands. The x-axis is detector, and the colors/symbols correspond to a particular RSB.
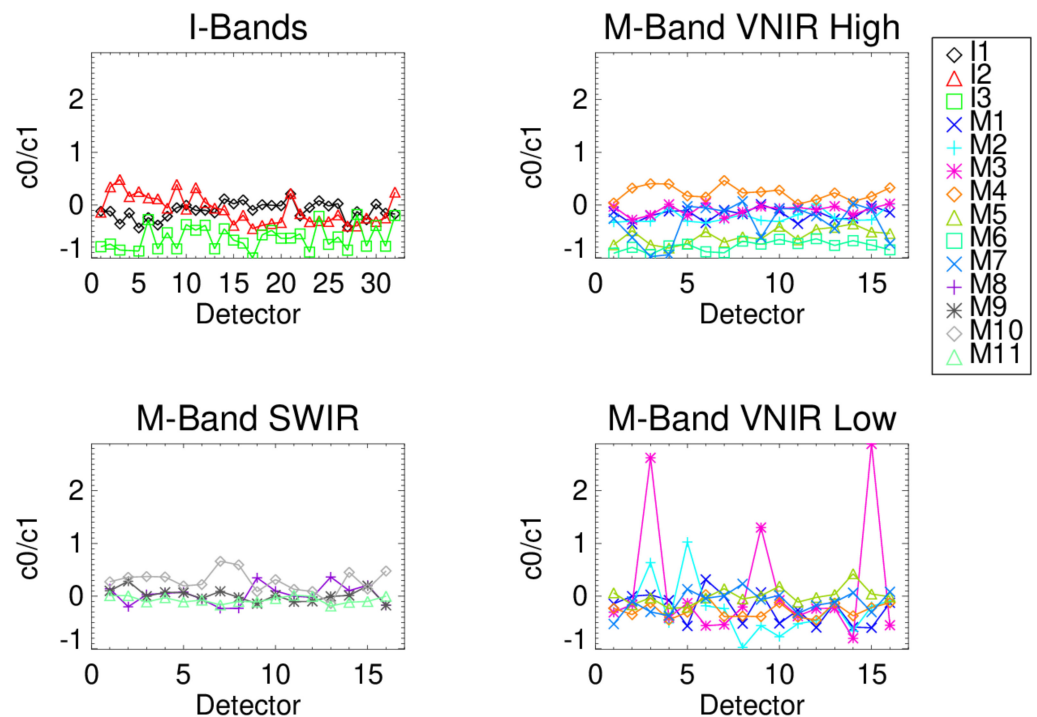

Figure 12. Comparison of the $\frac{c_0}{c_1}$ coefficient for all RSBs at nominal TVAC plateau. The upper left are the I-bands, upper right high gain VNIR M-bands, lower left the SWIR M-bands, and the lower right, the low gain VNIR M-bands. The x-axis is detector, and the colors/symbols correspond to a particular RSB.
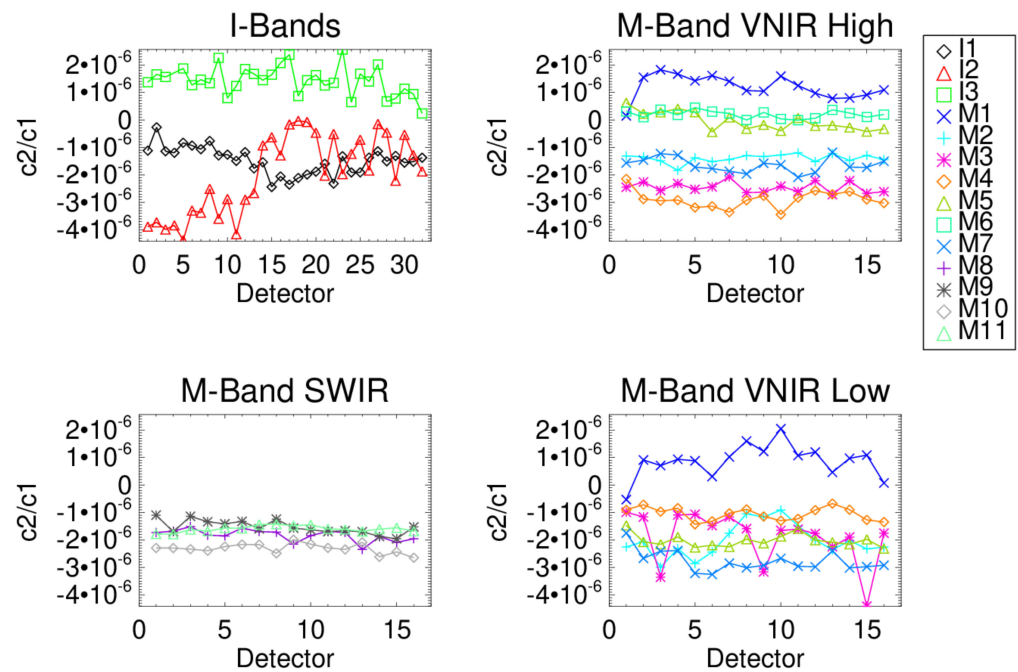
Figure 13. Comparison of the $\frac{c_2}{c_1}$ coefficient for all RSBs at nominal TVAC plateau. The upper left are the I-bands, upper right high gain VNIR M-bands, lower left the SWIR M-bands, and the lower right the low gain VNIR M-bands. The x-axis is detector, and the colors/symbols correspond to a particular RSB.

Table 5. JPSS-2 VIIRS c_1 calibration coefficient for each RSB gain stage and TVAC plateau at the primary electronics setting. The left, middle, and right sections are for cold, nominal and hot plateaus, respectively.

	Primary					
	Cold		**Nominal**		**Hot**	
Detector	**HG or SG**	**LG**	**HG or SG**	**LG**	**HG or SG**	**LG**
M1	0.3118	0.3152	0.3175	0.3200	0.3247	0.3262
M2	0.2611	0.2621	0.2655	0.2655	0.2687	0.2692
M3	0.2713	0.2717	0.2749	0.2751	0.2766	0.2770
M4	0.2299	0.0272	0.2325	0.0273	0.2349	0.0274
M5	0.2764	0.2768	0.2796	0.2796	0.2830	0.2831
M6	0.0131	-	0.0133	-	0.0133	-
M7	0.1168	0.1168	0.1185	0.1186	0.1193	0.1194
M8	0.0410	-	0.0412	-	0.0407	-
M9	0.0291	-	0.0259	-	0.0256	-
M10	0.0252	-	0.0251	-	0.0251	-
M11	0.0100	-	0.0100	-	0.0099	-
I1	0.2442	-	0.2455	-	0.2473	-
I2	0.1152	-	0.1163	-	0.1169	-
I3	0.0258	-	0.0257	-	0.0257	-
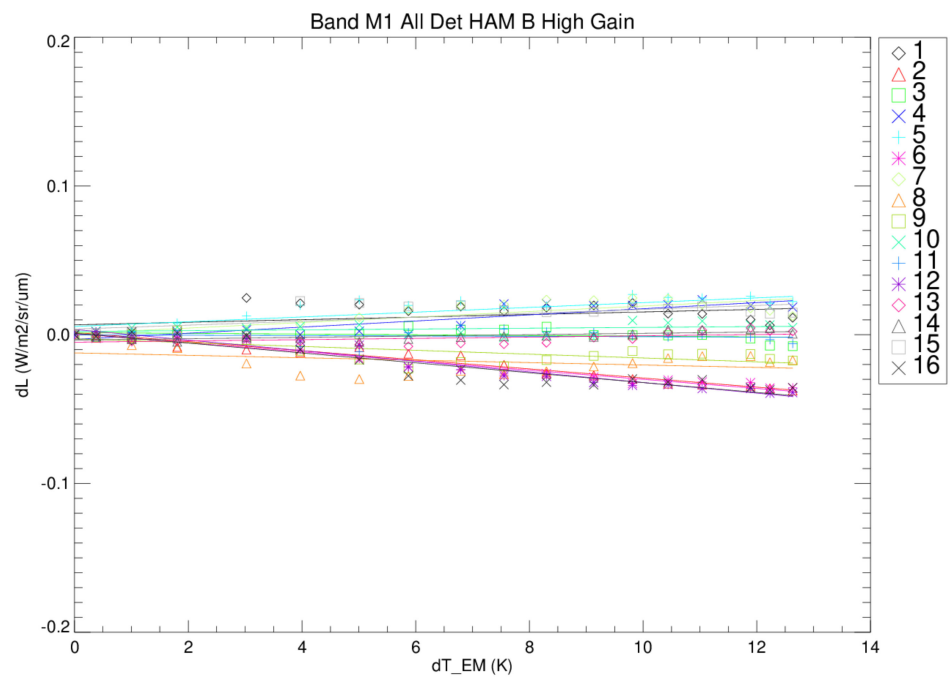
Figure 14. Band M1 temperature sensitivity (dL) as a function of electronics module (EM) temperature change between nominal and hot plateau for each detector (colors and symbols).
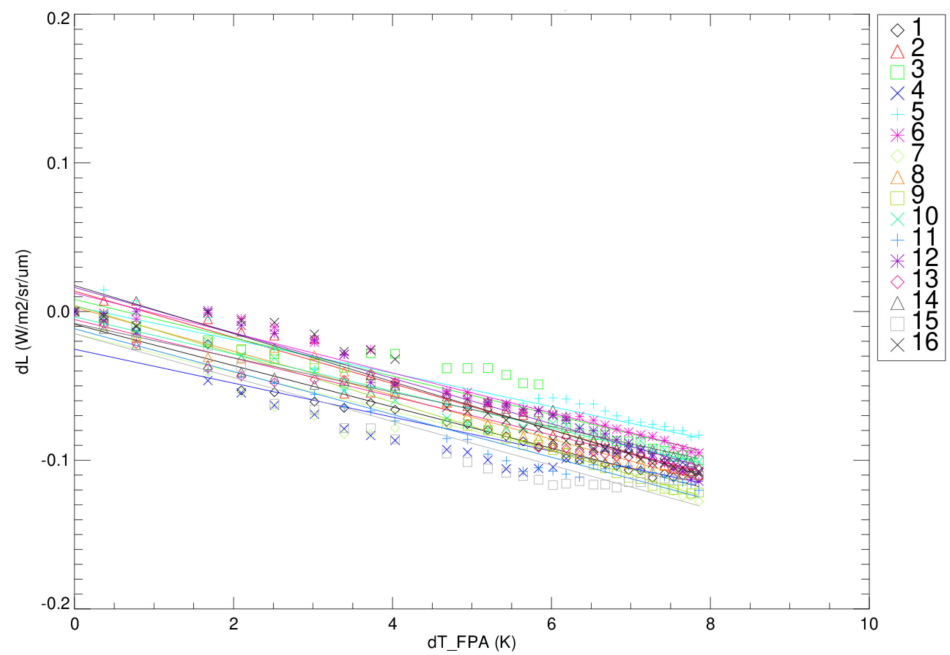
Figure 15. Band M1 temperature sensitivity (dL) as a function of focal plane assembly (FPA) temperature change between nominal and hot plateau for each detector (colors and symbols).

Table 6. JPSS-2 VIIRS radiometric sensitivity to temperature change of the instrument. Columns 2 and 3 are for electronics module and optomechanical module temperature sensitivities for the TVAC transition from cold to nominal plateaus and columns 4 and 5 are the corresponding sensitivities for the nominal to hot plateau transition.

	Cold-to-Nominal		Nominal-to-Hot	
	dL/dT EM	**dL/dT OMM**	**dL/dT EM**	**dL/dT OMM**
I1	−0.0011	−0.0063	0.0002	−0.0072
I2	−0.0016	−0.0060	0.0004	−0.0083
I3	0.0123	−0.0031	0.0004	−0.0014
M1	−0.0051	0.0015	0.0001	−0.0024
M2	0.0015	0.0002	0.0008	−0.0011
M3	0.0000	−0.0018	0.0004	−0.0021
M4	0.0002	−0.0031	0.0004	−0.0035
M5	−0.0014	−0.0090	0.0000	−0.0100
M6	−0.0008	−0.0029	0.0004	−0.0037
M7	0.0012	−0.0067	0.0003	−0.0078
M8	0.0047	−0.0018	0.0011	−0.0015
M9	−0.0069	0.0029	−0.0029	0.0028
M10	0.0126	−0.0036	0.0005	−0.0015
M11	0.0161	−0.0026	0.0006	0.0002

3.6. Uncertainty

The RSB reflectance uncertainty is broken down into six contributors to the total uncertainty. Figure 16 shows the reflectance accuracy error tree contributors that are combined using a root sum square (RSS) into the top-level accuracy value. Each one of the boxes in Figure 16 has subcategories that are listed in Table 7 for all the RSBs. The values in Table 7 come from subassembly measurements (SD, SDSM), modeled data (Lunar, straylight, end-of-life degradation) and pre-launch instrument measurements. The main contributor to the on-orbit reflectance accuracy is the uncertainty in the SD bi-directional reflectance factor (BRF) and the ability of the SDSM to track the change in the BRF. All the bands meet the 2% reflectance accuracy uncertainty requirement except for band M1. The band M1 RVS degradation over the mission and the OOB response in the SDSM are the main contributors to the 2.3% uncertainty noncompliance. The pre-launch calibration coefficient characterization uncertainty discussed in previous sections is a small contributor to the overall radiometric uncertainty. This is a testament to the pre-launch calibration test equipment and measurement methodology.
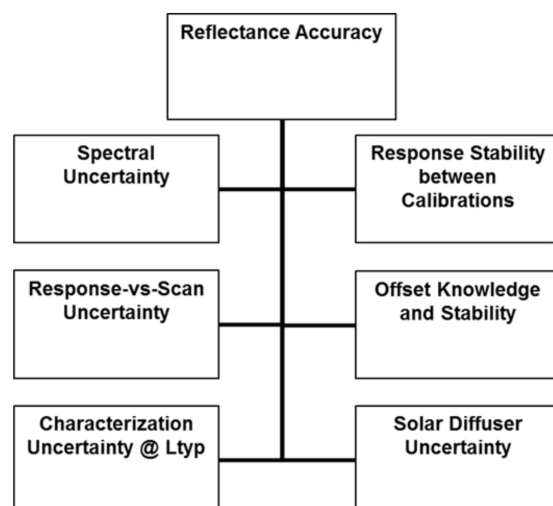
Figure 16. VIIRS top level radiometric calibration uncertainty tree.

Table 7. A breakout of the reflective solar band calibration uncertainty tree for each component as well as a total rollup (highlighted in green for pass and red for fail). The gray rows are headers with the rows below them the uncertainties associated with that item. Band M1 fails due to high uncertainty in the SDSM OOB spectral leak and the RVS change over the mission.

Description	Error Type	M1 Low	M1 High	M2 Low	M2 High	M3 Low	M3 High	M4 Low	M4 High	M5 Low	M5 High	M6	M7 Low	M7 High	M8	M9	M10	M11	I1	I2	I3
Reflectance Accuracy (RSS of Bias & Random Totals)		2.36	2.30	1.58	1.53	1.57	1.28	1.34	1.31	1.42	1.42	1.45	1.51	1.54	1.45	1.42	1.41	1.60	1.40	1.50	1.43
Characterization Uncertainty at Ltyp	Random	0.55	0.19	0.41	0.02	0.90	0.10	0.46	0.37	0.47	0.48	0.38	0.29	0.44	0.34	0.09	0.15	0.18	0.34	0.21	0.13
Response Stability	Random	0.137	0.137	0.126	0.126	0.118	0.118	0.118	0.118	0.129	0.129	0.120	0.118	0.118	0.171	0.150	0.140	0.130	0.413	0.161	0.138
Offset Knowledge & Stability	Random	0.050	0.021	0.030	0.020	0.040	0.016	0.030	0.021	0.050	0.049	0.052	0.050	0.027	0.117	0.082	0.052	0.168	0.175	0.083	0.170
Spec Unc Alloc	Random	0.00	0.00	0.00	0.00	0.00	0.00	0.00		0.00	0.00	0.00	0.00	0.00	0.00	0.00	0.00	0.00	0.00	0.00	0.00
RVS Unc Alloc																					
Pre-Launch Char Uncer	Random	0.07	0.07	0.04	0.04	0.04	0.04	0.04	0.04	0.03	0.03	0.02	0.02	0.02	0.02	0.10	0.03	0.02	0.03	0.03	0.03
Polarization Error	Random	0.00	0.00	0.00	0.00	0.00	0.00	0.00	0.00	0.00	0.00	0.00	0.00	0.00	0.00	0.00	0.00	0.00	0.00	0.00	0.00
RVS Change over Life	Random	1.37	1.37	0.65	0.65	0.20	0.20	0.00	0.00	0.10	0.10	0.00	0.10	0.10	0.08	0.08	0.04	0.07	0.10	0.10	0.04
SD Uncertainty																					
Pre-Launch SD BRDF	Random	0.91	0.91	0.91	0.91	0.91	0.91	0.91	0.91	0.91	0.91	0.91	0.91	0.91	0.91	0.91	0.91	0.91	0.91	0.91	0.91
Straylight	Bias	−0.61	−0.61	−0.61	−0.61	−0.61	−0.61	−0.61	−0.61	−0.61	−0.61	−0.61	−0.61	−0.61	−0.61	−0.61	−0.61	−0.61	−0.61	−0.61	−0.61
M11 BRDF Extrapolation	Random	0.00	0.00	0.00	0.00	0.00	0.00	0.00	0.00	0.00	0.00	0.00	0.00	0.00	0.00	0.00	0.00	1.70	0.00	0.00	0.00
Other SD																					
SD Degradation over Life	Random	0.12	0.07	0.13	0.07	0.10	0.04	0.10	0.04	0.10	0.04	0.04	0.09	0.03	0.09	0.13	0.09	0.16	0.08	0.10	0.20
SD—Sun Angle Uncertainty	Random	0.30	0.30	0.30	0.30	0.30	0.30	0.30	0.30	0.30	0.30	0.30	0.30	0.30	0.30	0.30	0.30	0.30	0.30	0.30	0.30
Post-Launch BRF Change	Random	0.50	0.50	0.50	0.50	0.50	0.50	0.50	0.50	0.50	0.50	0.50	0.50	0.50	0.50	0.50	0.50	0.50	0.50	0.50	0.50
SAS Error	Random	0.17	0.17	0.17	0.17	0.17	0.17	0.17	0.17	0.17	0.17	0.17	0.17	0.17	0.17	0.17	0.17	0.17	0.17	0.17	0.17
SDSM Error																					
Baseline SDSM Test	Random	0.61	0.61	0.61	0.61	0.61	0.61	0.61	0.61	0.61	0.61	0.61	0.61	0.61	0.61	0.61	0.61	0.61	0.61	0.61	0.61
Spectral OOB	Bias	1.94	0.19	1.17	1.17	0.73	0.73	0.61	0.61	0.17	0.17	0.01	−0.15	−0.15	0.00	0.00	0.00	0.00	0.39	−0.15	0.00

4. Discussion and Future Work

The pre-launch characterization of the RSB response discussed above is used in the on-orbit calibrated SDR products. These SDRs are key inputs into the weather and climate EDR products and require accurate calibration. Characterization of the calibration coefficients, SD BRDF, SAS and SDSM are key inputs into the calibrated RSB SDRs that have a 2% uncertainty requirement. The calibration coefficients use coefficient ratios to characterize the shape of the detector response. The SD BRDF is characterized to a NIST traceable standard and is used on-orbit to scale the calibration coefficients to obtain the absolute calibration. The SDSM and lunar vicarious calibration are used to track the degradation of the SD BRDF over the mission. Early on-orbit intensive calibration and validation activities will be performed to assess the quality of the pre-launch calibration coefficients, SD, and SDSM characterizations. This includes F and H factor trending, VIIRS sensor intercomparisons, and lunar calibrations to look for biases and stability issues. Image quality assessments for striping, cross-track banding, and crosstalk are performed to evaluate the RVS and calibration coefficient consistency over detector and HAM side, as well as look for unexpected response characteristics not captured in the prelaunch characterization activities. The high-to-low gain transition point for the dual gain bands will be examined to verify there is a smooth transition between gains. The VIIRS SDR calibration team will also work with the EDR community in their performance assessments to make sure the SDR product is providing adequate inputs into their EDR algorithms.

Another JPSS-2 VIIRS activity that will be performed during early on-orbit intensive calibration and validation is the VIIRS RSB radiance bias between sensor builds. The S-NPP and JPSS-1 VIIRS show a consistent bias between the RSBs of ~2–4% [23]. Sensor intercomparisons of JPSS-2 VIIRS with the previous two VIIRS builds will provide information on which sensor's calibration may be biased. The investigation in [24] suggests that the characterization of the SD BRDF is the main driver of the bias between S-NPP and JPSS-1 VIIRS. The SD BRDF of JPSS-2 VIIRS was characterized using the same ground test equipment and methodology as JPSS-1 VIIRS. If JPSS-1 and JPSS-2 VIIRS show good agreement and S-NPP VIIRS is the outlier, then the SD BRDF may be the root cause of the VIIRS sensor biases.

5. Conclusions

The JPSS-2 VIIRS reflective solar band radiometric performance was evaluated prelaunch during TVAC testing at three different temperature plateaus. The dynamic range, signal-to-noise ratio, dual gain switching, gain temperature sensitivity and calibration coefficient characterization was discussed. Band M8 failed to meet the dynamic range requirements but is an improvement over JPSS-1 where bands M8 and I3 both failed requirements. Bands I3 and M6 have saturation rollover effects that can impact the SDR performance at very bright scenes. This was also present in S-NPP and JPSS-1 VIIRS and has an SDR correction algorithm to mitigate its impact. The SNRs for all bands meet the requirements with no out-of-family detectors observed (JPSS-1 had one bad detector). All the RSBs meet their calibration coefficient uncertainty requirements, as seen in Table 7. The calibration coefficient fits are assessed based on their 2-sigma uncertainties to optimize their performance on-orbit. This included forcing the offset coefficient to zero and fixing the transmission of the prelaunch attenuator screen across detector to improve the consistency of the second order fit coefficient across detector. The radiometric uncertainty of the RSBs is within the 2% requirements except for band M1. This is due to UV degradation of the optics and SD over the instrument's mission life. This causes the end-of-life RVS and SD BRF uncertainty to increase, causing a requirements failure. While not a requirement, the temperature sensitivity of the detector's response was characterized. The sensitivity was shown to be small with the EM temperature having little effect on detector response and the OMM temperature being the main driver of temperature-dependent detector response change. These temperature effects are included in the on-orbit SDR calibration coefficient LUTs to reduce calibration uncertainty within an orbit and over different seasons.

References

1. Xiong, X.; Aldoretta, E.; Angal, A.; Chang, T.; Geng, X.; Link, D.; Salomonson, V.; Twedt, K.; Wu, A. Terra MODIS: 20 years of on-orbit calibration and performance. *J. Appl. Rem. Sens.* **2020**, *14*, 037501. [CrossRef]
2. Xiong, X.; Wenny, B.N.; Barnes, W.L. Overview of NASA Earth Observing Systems Terra and Aqua Moderate Resolution Imaging Spectroradiometer Instrument Calibration Algorithms and On-orbit Performance. *J. Appl. Remote Sens.* **2009**, *3*, 032501.
3. Cao, C.; De Luccia, F.; Xiong, X.; Wolfe, R.; Weng, F. Early On-Orbit Performance of the Visible Infrared Imaging Radiometer Suite Onboard the Suomi National Polar-Orbiting Partnership (S-NPP) Satellite. *IEEE Trans. Geosci. Remote Sens.* **2013**, *52*, 1142–1156. [CrossRef]
4. Choi, T.; Cao, C.; Blonski, S.; Wang, W.; Uprety, S.; Shao, X. NOAA-20 VIIRS Reflective Solar Band Postlaunch Calibration Updates Two Years In-Orbit. *IEEE Trans. Geosci. Remote Sen.* **2020**, *58*, 7633–7642. [CrossRef]
5. Holben, B.N.; Kaufman, Y.J.; Kendall, J.D. NOAA-11 AVHRR visible and near-IR inflight calibration. *Int. J. Remote Sens.* **1990**, *11*, 1511–1519. [CrossRef]
6. Salomonson, V.V.; Barnes, W.; Xiong, J.; Kempler, S.; Masuoka, E. An overview of the Earth Observing System MODIS instrument and associated data systems performance. In Proceedings of the IEEE International Geoscience and Remote Sensing Symposium, Toronto, ON, Canada, 24–28 June 2002; Volume 2, pp. 1174–1176.
7. Moeller, C.; Schwarting, T.; McCorkel, J.; Moyer, D.; McIntire, J. JPSS-2 VIIRS version 2 at-launch relative spectral response characterization. In Proceedings of the SPIE, Earth Observing Systems XXIV, San Diego, CA, USA, 9 September 2019; Volume 11127, p. 111270D. [CrossRef]
8. Baker, N.; Kilcoyne, H. *Joint Polar Satellite System (JPSS) VIIRS Radiometric Calibration Algorithm Theoretical Basis Document (ATBD)*; Goddard Space Flight Center: Greenbelt, MA, USA, 2013.
9. Liu, Y.; Yu, Y.; Yu, P.; Göttsche, F.M.; Trigo, I.F. Quality Assessment of S-NPP VIIRS Land Surface Temperature Product. *Remote Sens.* **2015**, *7*, 12215–12241. [CrossRef]
10. Patt, F.S.; Feldman, G.C. VIIRS Product Evaluation at the Ocean PEATE. In Proceedings of the 2010 IEEE International Geoscience and Remote Sensing Symposium, Honolulu, HI, USA, 25–30 July 2010; pp. 300–303. [CrossRef]
11. Frey, R.A.; Ackerman, S.A.; Holz, R.E.; Dutcher, S.; Griffith, Z. The Continuity MODIS-VIIRS Cloud Mask. *Remote Sens.* **2020**, *12*, 3334. [CrossRef]
12. Lu, X.; Zhang, X.; Li, F.; Cochrane, M.A.; Ciren, P. Detection of Fire Smoke Plumes Based on Aerosol Scattering Using VIIRS Data over Global Fire-Prone Regions. *Remote Sens.* **2021**, *13*, 196. [CrossRef]
13. Xiong, X.; Butler, J.; Chiang, K.; Efremova, B.; Fulbright, J.; Lei, N.; McIntire, J.; Oudrari, H.; Sun, J.; Wang, Z.; et al. VIIRS on-orbit calibration methodology and performance. *J. Geophys. Res. Atmos.* **2014**, *119*, 5065–5078. [CrossRef]
14. Xiong, X.; Sun, J.; Angal, A.; Wilson, T. Calibration Inter-Comparison of MODIS and VIIRS Reflective Solar Bands Using Lunar Observations. *Remote Sens.* **2022**, *14*, 4754. [CrossRef]
15. Choi, T.; Shao, X.; Cao, C. On-orbit radiometric calibration of Suomi NPP VIIRS reflective solar bands using the Moon and solar diffuser. *Appl. Opt.* **2018**, *57*, 9533–9542. [CrossRef] [PubMed]
16. Wang, W.; Cao, C. NOAA-20 and S-NPP VIIRS Thermal Emissive Bands On-Orbit Calibration Algorithm Update and Long-Term Performance Inter-Comparison. *Remote Sens.* **2021**, *13*, 448. [CrossRef]
17. Thuillier, G.; Hersé, M.; Labs, D.; Foujols, T.; Peetermans, W.; Gillotay, D.; Simon, P.C.; Mandel, H. The Solar Spectral Irradiance from 200 to 2400 nm as Measured by the SOLSPEC Spectrometer from the Atlas and Eureca Missions. *Sol. Phys.* **2003**, *214*, 1–22. [CrossRef]
18. Murgai, V.; Johnson, L.; Klein, S. Spectralon solar diffuser BRDF variation for NPP, JPSS J1 and J2. In *Earth Observing Systems XXII*; SPIE: Bellingham, WA, USA, 2017; Volume 10402. [CrossRef]
19. McIntire, J.; Moyer, D.; Chang, T.; Oudrari, H.; Xiong, X. Pre-Launch JPSS-2 VIIRS Response versus Scan Angle Characterization. *Remote Sens.* **2017**, *9*, 1300. [CrossRef]

20. Moeller, C.; McIntire, J.; Schwarting, T.; Moyer, D.; Costa, J. Suomi NPP VIIRS spectral characterization: Understanding multiple RSR releases. In Proceedings of the SPIE, Earth Observing Systems XVII, San Diego, CA, USA, 15 October 2012; Volume 8510, p. 85101S. [CrossRef]

21. Oudrari, H.; McIntire, J.; Xiong, X.; Butler, J.; Ji, Q.; Schwarting, T.; Angal, A. An Overall Assessment of JPSS-2 VIIRS Radiometric Performance Based on Pre-Launch Testing. *Remote Sens.* **2018**, *10*, 1921. [CrossRef]

22. Moyer, D.; De Luccia, F.; Haas, E. JPSS-1 VIIRS reflective solar band on-orbit calibration performance impacts due to SWIR nonlinearity artifacts. In Proceedings of the SPIE, Sensors, Systems, and Next-Generation Satellites XX, Edinburgh, UK, 19 October 2016; Volume 10000. [CrossRef]

23. Jing, X.; Uprety, S.; Liu, T.-C.; Zhang, B.; Shao, X. Evaluation of SNPP and NOAA-20 VIIRS Datasets Using RadCalNet and Landsat 8/OLI Data. *Remote Sens.* **2022**, *14*, 3913. [CrossRef]

24. Moyer, D.; Uprety, S.; Wang, W.; Cao, C.; Guch, I. S-NPP/NOAA-20 VIIRS reflective solar bands on-orbit calibration bias investigation. In Proceedings of the SPIE, Earth Observing Systems XXVI, San Diego, CA, USA, 3 August 2021; Volume 11829, p. 1182912. [CrossRef]